frontiers in Mechanical Engineering

ORIGINAL RESEARCH
published: 12 August 2021
doi: 10.3389/fmech.2021.739914

Ultrafine Particulate Matter in Methane-Air Premixed Flames With Oxygen Enrichment

Shruthi Dasappa[1,2] *and Joaquin Camacho*[2]*

[1]Mechanical and Aerospace Engineering Department, University of California San Diego, San Diego, CA, United States, [2]Mechanical Engineering Department, San Diego State University, San Diego, CA, United States

A complementary computational and experimental study is carried out on the formation of ultrafine particulate matter in premixed laminar methane air flames. Specifically, soot formation is examined in premixed stretch-stabilized flames to observe soot inception and growth at relatively high flame temperatures common to oxygen enriched applications. Particle size distribution functions (PSDF) measured by mobility sizing show clear trends as the equivalence ratio increases from $\Phi = 2.2$ to $\Phi = 2.4$. For a given equivalence ratio, the measured distribution decreases in median mobility particle size as the maximum flame temperature increases from approximately 1,950–2,050 K. The median mobility particle size is 20 nm or less for all flame conditions studied. The volume fraction decreases with increasing flame temperature for all equivalence ratio conditions. The $\Phi = 2.2$ condition is close to the soot inception limit and both number density and volume fraction decrease monotonically with increasing flame temperature. The higher equivalence ratio conditions show a peak in number density at 2,000 K which may indicate competing soot inception processes are optimized at this temperature. Flame structure computations are carried out using detailed gas-phase combustion chemistry of the Appel, Bockhorn, Frenklach (ABF) model to examine the connection of the observed PSDF to soot precursor chemistry. Agreement between measured and computed flame standoff distances indicates that the ABF model could provide a reasonable prediction of the flame temperature and soot precursor formation for the flames currently studied. To the first order, the trends observed in the measured PSDF could be understood in terms of computed trends for the formation of benzene, naphthalene and other soot precursors. Results of the current study inform particulate matter behavior for methane and natural gas combustion applications at elevated temperature and oxygen enriched conditions.

Keywords: soot, carbon, methane, particulate matter, particle size distibution, enriched air

OPEN ACCESS

Edited by:
Chiara Saggese, United States Department of Energy (DOE), United States

Reviewed by:
Carson Chu, University of Toronto, Canada
Gianluigi De Falco, DICMAPI - University of Naples Federico II, Italy
Francesco Carbone, University of Connecticut, United States

***Correspondence:**
Joaquin Camacho
jcamacho@sdsu.edu

Specialty section:
This article was submitted to Engine and Automotive Engineering, a section of the journal Frontiers in Mechanical Engineering

Received: *12 July 2021*
Accepted: *03 August 2021*
Published: *12 August 2021*

Citation:
Dasappa S and Camacho J (2021) Ultrafine Particulate Matter in Methane-Air Premixed Flames With Oxygen Enrichment. Front. Mech. Eng 7:739914. doi: 10.3389/fmech.2021.739914

INTRODUCTION

Particulate matter formation is a crucial factor for combustion applications affecting performance (Heywood, 2018), emissions regulations (Jacobson, 2001) and public health (Jacobson et al., 2000). The most prominent particle produced in conventional combustion engines is soot originating from fuel-rich pockets. As such, a major thrust of combustion research is to develop fundamental knowledge of soot formation processes to minimize negative impacts. Natural gas is an important fuel for transportation, heating and process applications with recent boost in the United States from

TABLE 1 | Summary of flame conditions currently studied.

Flame	Φ	T_{fmax}[a] (K)	X_{CH4}	X_{O2}	X_{N2}	V_o[b] (cm/s)	t_p[a] (ms)
2.2a	2.23	1,980	0.323	0.289	0.388	32.5	16
2.2b	2.23	2,010	0.349	0.313	0.364	31.2	15
2.2c	2.23	2,050	0.365	0.327	0.338	30.0	14
2.2d	2.23	2,095	0.365	0.327	0.308	28.7	14
2.3a	2.33	1,980	0.354	0.304	0.343	29.6	17
2.3b	2.33	2,025	0.370	0.318	0.312	28.3	16
2.3c	2.33	2,040	0.378	0.325	0.297	27.7	16
2.4a	2.43	1,965	0.383	0.316	0.301	27.4	18
2.4b	2.43	1,980	0.399	0.329	0.272	26.3	17
2.4c	2.43	2,050	0.420	0.347	0.233	24.9	16

[a]*Computed from OPPDIF based on T_{nozzle} = 300 K, T_{plate} = 473 K and nozzle-to-stagnation L = 1.5 cm.*
[b]*Cold gas velocity.*

hydraulic fracturing resources (Montgomery and Smith, 2010). Oxygen enriched conditions are often used with natural gas to optimize heat transfer and emissions performance (Shaddix and Williams, 2017). The current study examines soot formation in premixed methane—enriched air flames using modeling and experimental approaches. Insights into soot inception and growth are gained for these conditions by measuring particle size distributions in the smallest particle size range. Studies on flame structure effects (Xu et al., 1997; Alfè et al., 2010), parent fuel effects (Slavinskaya and Frank, 2009; Sirignano et al., 2011; Russo et al., 2013), and soot inception (Desgroux et al., 2017; Mouton et al., 2013; D'Anna et al., 2008) have been reported for premixed methane flames but the current study focuses on ultrafine (<100 nm) particle formation at elevated flame temperatures under oxygen enrichment. Maricq introduced probe sampling methods and addressed challenges for analysis of mobility size distributions in premixed flames (Maricq et al., 2003; Maricq, 2004; Maricq, 2006). Ever since several investigators have provided useful particle size experimental observations including extensions into particle sizes approaching 1 nm (Wang et al., 2014; Carbone et al., 2016; Carbone et al., 2017a; Carbone et al., 2017b; Tang et al., 2017; Larriba-Andaluz and Carbone, 2021). The current work uses the latest TSI mobility sizing system to examine mobility size down to 1 nm.

Premixed stretch-stabilized flames are established by an aerodynamic balance rather than anchoring by heat loss (Law, 2006) which enables temperatures approaching the adiabatic flame temperature. This configuration is applied in the current study to examine soot formation at elevated temperatures common under oxygen enrichment. Stretch-stabilized stagnation flames also enable systematic probe sampling under well-defined boundary conditions (Camacho et al., 2017; Bonpua et al., 2019; Dasappa and Camacho, 2021a; Dasappa and Camacho, 2021b). Flow perturbations at the sampling orifice are unavoidable but the stagnation surface is an explicit boundary that facilitates complementary modeling to account for probe effects on measured properties (Camacho et al., 2015a; Saggese et al., 2016; Brunnenmeyer and Camacho, 2019). The time for particle growth could be reduced by up to 20% in these flames depending on the orifice and applied pressure drop (Dasappa and Camacho, 2021c). With this in mind, flame structure modeling is carried out to interpret the observed soot formation behavior in terms of flame structure effects and soot precursor chemistry.

MATERIALS AND METHODS

Experimental Methods

A series of methane-air flames with oxygen enrichment is designed to systematically observe the effects of flame temperature and equivalence ratio on soot formation in premixed laminar flames. Flame conditions spanning $2.2 < \Phi < 2.4$ and $1{,}965\ K < T_{f,max} < 2{,}095\ K$ are summarized in **Table 1**. The nozzle-to-stagnation surface separation distance is L = 1.5 cm for all flames studied and the computed particle time ($t_p \sim 15$ ms) is also comparable for all flames. The particle time can be considered to be the residence time for a particle nucleated at the flame zone and sampled at the stagnation surface. For a given equivalence ratio, the flame temperature is adjusted by independently adjusting the flow rate of diluent nitrogen gas fed to the flame. The experimental setup, summarized in **Figure 1**, centers upon an aerodynamic nozzle (D_{nozzle} = 1.43 cm) which issues the premixed fuel/air flow. The nozzle takes contours defined by Bergthorson (Bergthorson, 2005) to induce a plug flow at the nozzle boundary. A concentric flow of nitrogen surrounds the flame to reduce perturbation from the surrounding environment. The temperature at the nozzle and stagnation surface boundary are monitored by Type K thermocouples with temperatures maintained at T_{nozzle} = 330 ± 20 K and $T_{stagnation}$ = 473 ± 20 K. Calibrated critical orifices are used to control all gas flow rates with oxygen enrichment established by using independent oxygen and nitrogen gas supply.

A sample probe with orifice diameter of 130 micron is embedded into the stagnation surface with sampling procedures established to minimize particle diffusion losses and artificial coagulation (Abid et al., 2009a; Cain et al., 2011; Camacho et al., 2013; Puduppakkam et al., 2014; Camacho et al., 2015b; Saggese et al., 2019; Dasappa and Camacho, 2021d). Particle size is measured by mobility sizing using a TSI 1 nm Scanning Mobility Particle Sizer (TSI 3838E77, SMPS) in the "compact" configuration to minimize diffusion loss of the smallest particles. This SMPS system contains a dual voltage classifier (TSI 3082), a Kr-85 bi-polar diffusion charger (Neutralizer TSI 3077A), 1 nm differential mobility analyzer (DMA) (TSI 3086), a diethylene glycol-based (DEG) condensation particle counter (CPC) (so-called Nanoenhancer, TSI 3777) and a butanol-based CPC (TSI 3772). TSI Aerosol Instrument Manager Software (version 10.2) is used to collect and export the measured PSDFs. An insert supplied by the vendor is now mounted onto the inlet of the neutralizer to minimize flow recirculation for more predictable attainment of the equilibrium charge distribution. TSI also measured the penetration of ultra-fine particles through the system flow path recently and a new diffusion loss correction (TSI, 2019) is applied to the measured particle size distribution function (PSDF). The mobility size is corrected to properly account for the transition in gas-particle

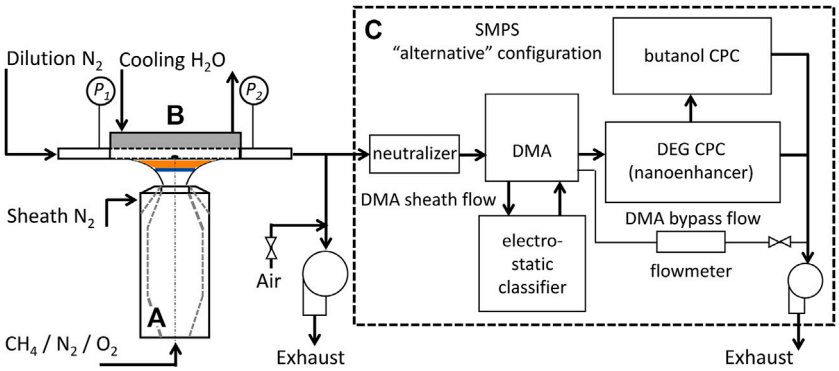

FIGURE 1 | Experimental setup including an aerodynamic nozzle for premixed flames **(A)**, a stagnation surface/sampling probe assembly **(B)**, and a TSI SMPS system in the compact configuration **(C)**.

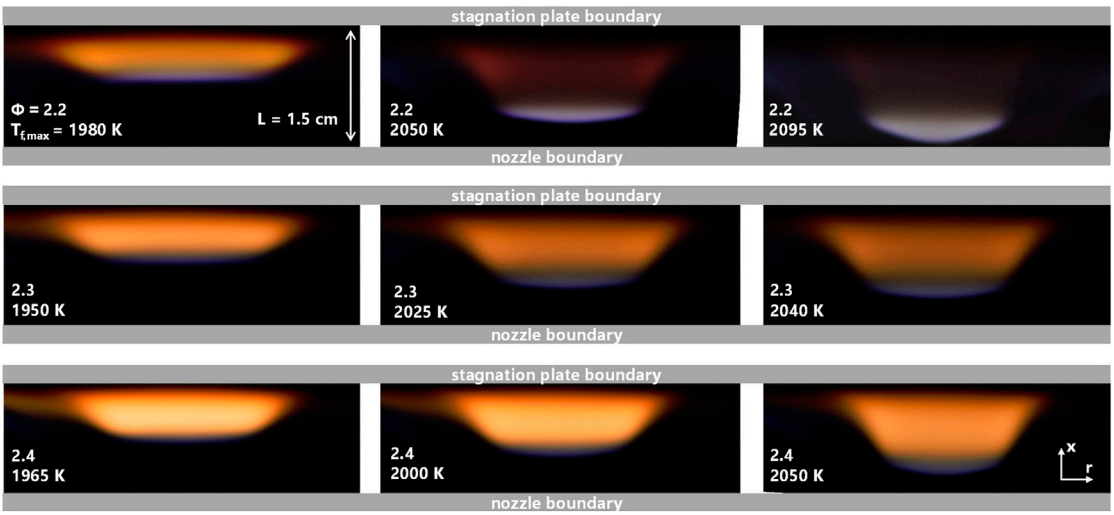

FIGURE 2 | Images for the series of flames currently studied.

collision regimes for ultra-fine soot particles (Li and Wang, 2003). The dilution ratio is calibrated using independent flow-meter and CO_2 detector measurements. As discussed previously (Zhao et al., 2003; Abid et al., 2009b; Camacho et al., 2015a; Gu et al., 2016; Lin et al., 2016), the dilution ratio is correlated to indicated pressure drop at the sample probe dilution flow inlet and outlet. The dilution ratio applied to all flames is 2,100 for the current study. The flame position is determined experimentally by analysis of flame projection images obtained from a Nikon D5300 DSLR camera.

Computational Methods

Premixed stretch-stabilized flames are a relatively simple axisymmetric flow field that can be solved using a similarity solution (Von Karman, 1921; Seshadri and Williams, 1978; Smooke et al., 1988; Kee et al., 1989a). Previous studies have indicated that the similarity solution is reasonably accurate for stretch-stabilized flames with a wide range of nozzle-to-stagnation surface separations (Saggese et al., 2015; Yapp et al., 2015; Liu et al., 2018; Dasappa and Camacho, 2020). The OPPDIF flame solver (Lutz et al., 1997) is used in the current study to compute the flame structure with a similarity solution in the Chemkin framework (Kee et al., 1989b). Detailed gas-phase combustion chemistry and transport is modeled with the Appel, Bockhorn, Frenklach (ABF) model (Appel et al., 2000) to examine flame structure and the effect of flame structure on production of PAH soot precursors. The current computations do not consider soot formation processes because extensive development of chemical reversibility, graphitization and other processes at elevated flame temperatures will be left to future work.

RESULTS AND DISCUSSION

Images of the series of flames currently studied are shown in **Figure 2**. The image is a projection of the axisymmetric

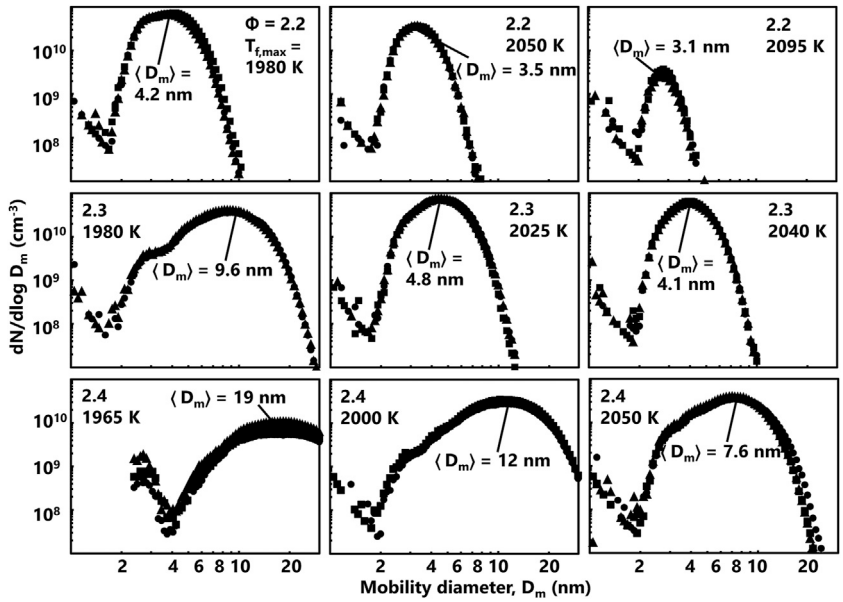

FIGURE 3 | Measured PSDF for the series of flames currently studied. The PSDF measurement is repeated three times and different symbols are used to highlight repeated measurements. The median diameter, <D_m>, is labeled for each flame condition as well.

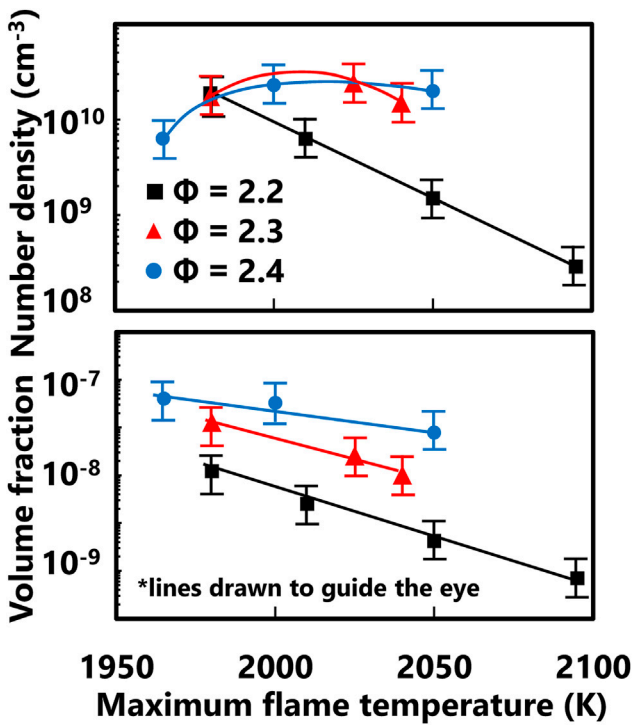

FIGURE 4 | Global particle distribution properties derived from the measured PSDF. Lines are drawn to guide the eye.

stagnation flow with a steady flame position indicated by the thin blue disc. For flames sitting close to the nozzle boundary, non-ideal deviations from the flat disc shape are observed due to the tendency of the flame to anchor. The intensity of the orange luminosity in the post-flame region is an indication of the amount of soot produced in the flame. As expected, the most intense luminosity is observed for the most fuel rich flames.

Measured PSDF for the series of flames currently studied is shown in **Figure 3**. For a given equivalence ratio, the median mobility particle size decreases as the flame temperature increases. This indicates that soot formation processes are hindered at elevated temperatures due to reversibility in precursor formation and soot growth (Alfè et al., 2010; Abid et al., 2008), increase in OH oxidation (Haynes and Wagner, 1981) and a reduction in coagulation efficiency (D'Alessio et al., 2005; Sirignano and D'Anna, 2013; Pejpichestakul et al., 2018; Raj et al., 2010). For comparable flame temperature, the median mobility diameter increases over a factor of two from $\langle D_m \rangle$ = 4.2–9.6 nm to 19 nm as the equivalence ratio increases incrementally from Φ = 2.2 to 2.3 to 2.4. With exception of the Φ = 2.4, $T_{f,max}$ = 1,965 K condition, the median mobility particle diameter is on the order of 10 nm and below. Global properties derived from the measured PSDF are shown in **Figure 4** for the series of flames currently studied. The number density is the area under curve for the measured number weighted PSDF but extraction of the volume fraction requires an assumption of the particle morphology. The measured mobility diameter is interpreted to correspond to spherical particles as evidence suggests for particles in the current size range (Camacho et al., 2015a; Appel et al., 2000; Schenk et al., 2013). For each mobility diameter bin, a volume weighting corresponding the sphere volume is applied and the volume fraction is the area under the volume weighted PSDF. For the lowest equivalence ratio condition, a clear downward trend in number density and volume fraction is observed as the flame

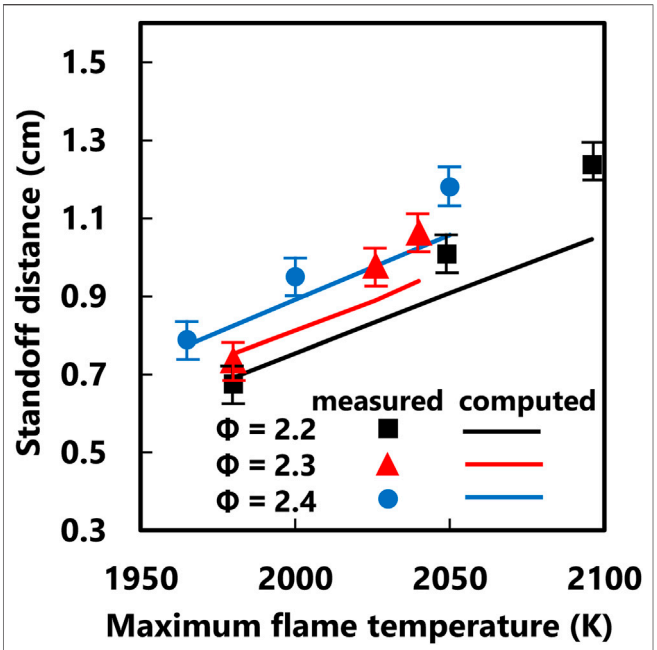

FIGURE 5 | Measured and computed flame standoff distance for the series of flames currently studied.

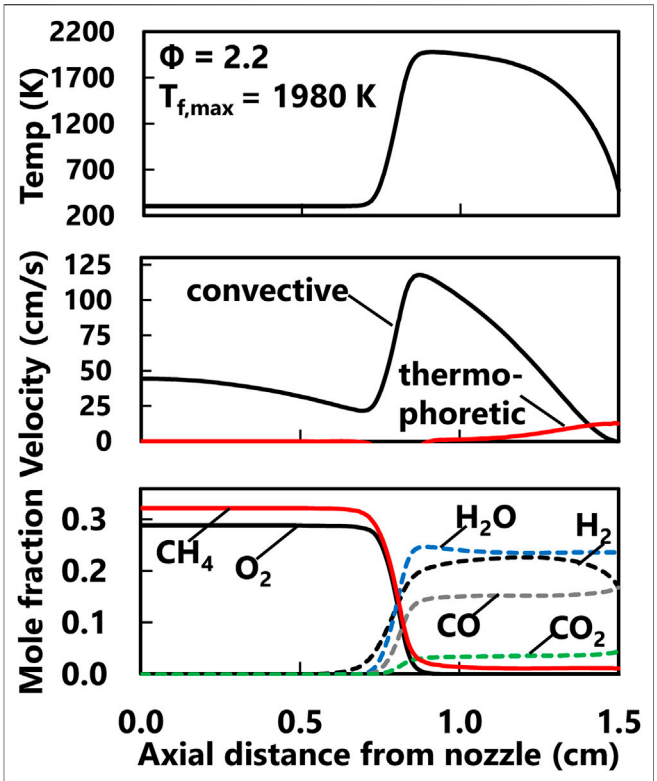

FIGURE 6 | Computed axial temperature profile **(top)**, axial velocity profiles **(middle)** and major products **(bottom)** at the centerline for the Φ = 2.2, $T_{f,max}$ = 1,980 K flame.

temperature increases. The higher equivalence ratio conditions also show decreasing volume fraction with increasing flame temperature, but the number density shows a broad peak in this temperature range. This broad peak in the number density but down trend in volume fraction may indicate that soot inception is optimal for 2,000 K flames but growth processes are favored at lower flame temperatures. A peak in global sooting properties is a known temperature dependent behavior reported ever since early flame (Böhm et al., 1989) and shock-tube studies (Frenklach et al., 1985). As **Figure 2** shows, the lowest equivalence ratio series is close the limit of visible soot luminosity. The downward trend for both number density and volume fraction in this case may indicate that soot inception is favored at lower temperature for sooting limit flame conditions. Experimental observation of the detailed PSDF for the earliest inception stages provides a valuable guide for developing soot formation models including recent hypotheses for soot inception (Commodo et al., 2015; Johansson et al., 2018; Bartos et al., 2019; Bowal et al., 2019; Gleason et al., 2021).

Complementary flame structure calculations are carried out for the series of flames currently studied. The flame standoff distance is considered to be the distance from the blue flame disc to the stagnation surface. This is measured in the current study from analysis of pixel intensities in the flame projection images. The computed flame standoff distance is considered to be the location of the peak CH* concentration in the centerline axial profile. A comparison between measured and computed values is shown in **Figure 5**. Reasonable agreement is observed as long as the flame does not approach the vicinity of the nozzle (high standoff distance). As discussed above, the flame disc distorts significantly for flame position close to the nozzle due to the tendency to anchor onto any solid surface. This effect causes a significant disagreement between the measured flame standoff distance for the Φ = 2.2, $T_{f,max}$ = 2,095 K condition. Reasonable agreement for the other conditions indicates that the ABF combustion chemistry model reasonably predicts the fuel burn rate and flame temperature. The delicate kinematic balance between opposing burning and flow velocity determines the flame position and the ABF model is able to capture the experimental behavior.

With the performance of the ABF model established for the current flames, the flame structure calculations could provide insight into temperature and flame chemistry effects. The computed flame structure for the Φ = 2.2, $T_{f,max}$ = 1,980 K case is shown in **Figure 6** to demonstrate the profiles for a typical premixed stretch-stabilized flame. The axial temperature profile shows the sharp temperature increase at the flame reaction zone significantly downstream of the nozzle exit. The axial convective velocity also increases at the flame and falls down to zero at the stagnation surface. The thermophoretic velocity of the soot particles is calculated based on the assumption that the particles follow the gas streamlines and the hard sphere approximation applies. Assuming inception of the first particles occurs at the flame reaction zone, the time for the particle to traverse the flame zone to the stagnation surface is comparable across all flames (see **Table 1**). The computed major species for this fuel rich flame show CO production is much

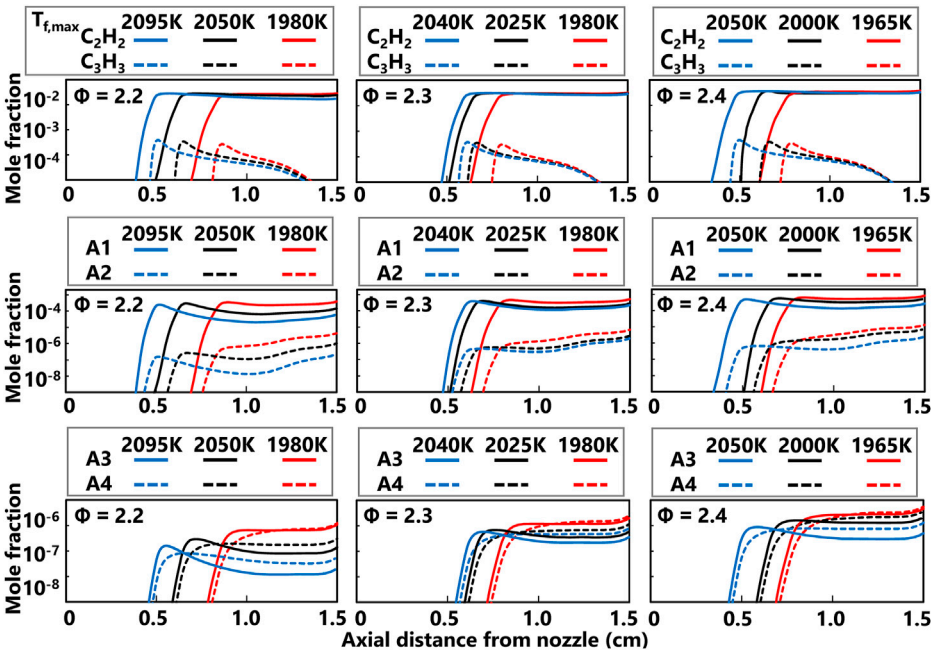

FIGURE 7 | Computed centerline axial profiles of soot precursors for the series of flames currently studied. The top row shows the production of acetylene (C2H2) and propargyl radical (C3H3), the middle row shows the production of benzene (A1) and naphthalene (A2), and the bottom row shows the production of phenanthrene (A3) and pyrene (A4).

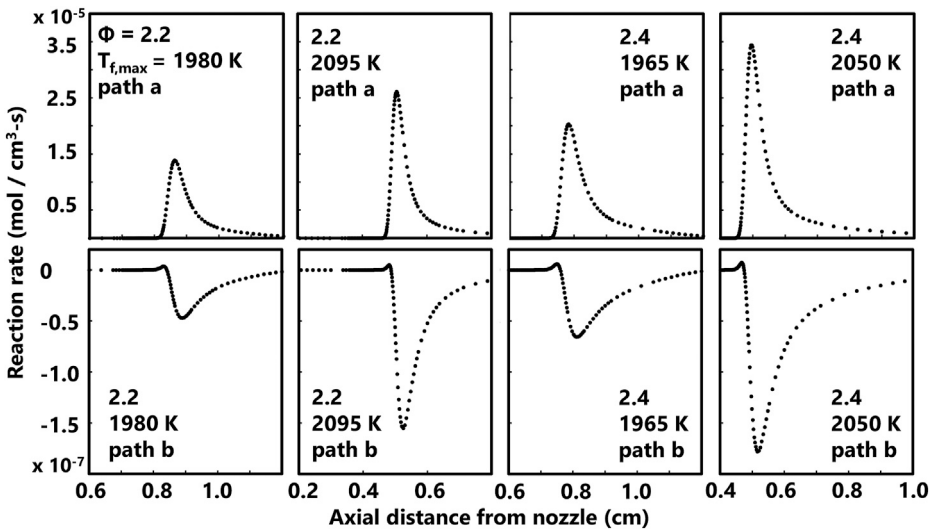

FIGURE 8 | Computed rates of two common benzene (A1) production reactions for four flames spanning the range of equivalence ratios and flame temperatures currently studied. The top row is the axial profile for the net rate of $2C_3H_3\bullet$ = A1 (path a) and the bottom row is the axial profile for the net rate of n-$C_4H_5\bullet$ + C_2H_2 = A1 + H● (path b).

higher than CO_2 but H_2 and H_2O are produced at comparable levels. Computed profiles for light and heavy soot precursors are shown in **Figure 7** for the series of flames currently studied. As **Table 1** shows, the computed particle residence times are all within 13% which effectively minimizes growth time effects on the measured PSDF and computed species profiles. Interestingly, the predicted concentrations of acetylene and propargyl radical are not substantially different across the current range of equivalence ratio and flame temperature. In contrast, the computed profiles for benzene and PAH predict concentrations show some sensitivity to the flame temperature. The measured volume fraction decreases with increasing flame

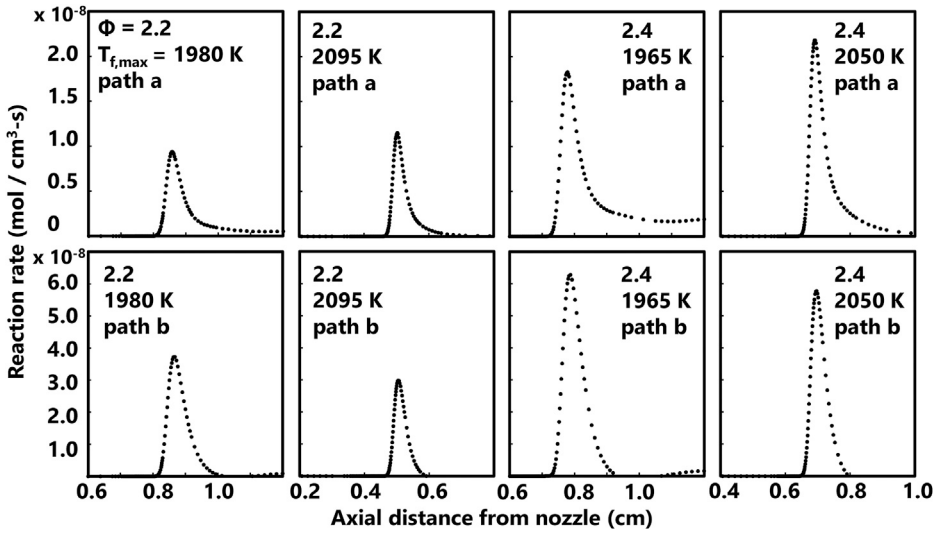

FIGURE 9 | Computed rates of two common naphthalene (A2) production reactions for four flames spanning the range of equivalence ratios and flame temperatures currently studied. The top row is the axial profile for the net rate of A1● + C_4H_4 = A2 + H● (path a) and the bottom row is the axial profile for the net rate of A2● + H● = A2 (path b).

temperature for all equivalence ratio series but the trends for computed PAH are not strong in all cases. For the Φ = 2.2 case, the computed A1-A4 profiles show a clear decreasing trend with increasing flame temperature. This downward trend is generally true for the Φ = 2.3 case but narrower range in flame temperature results in a narrower spread in predicted concentrations. The highest equivalence ratio conditions show a relatively weak sensitivity of the computed A1-A4 mole fractions even though the predicted range of temperatures is wider.

Reaction rates predicted by the ABF model are also shown here to provide insight into soot precursor formation pathways. Computed profiles for rates of propargyl recombination ($2C_3H_3$● = A1) and acetylene + butadienyl (n-C_4H_5● + C_2H_2 = A1 + H●) is shown in **Figure 8** for four flames spanning the range of equivalence ratios and flame temperatures currently studied. The most significant reaction pathway for benzene production is propargyl recombination for the current series of methane flames. As shown in **Figure 8**, the C_2 pathway is not favored as the reverse reaction consumes a small fraction of benzene in the flame. Predicted production rates for naphthalene based on the A1● + C_4H_4 = A2 + H● pathway and the A2● + H● = A2 pathway are shown in **Figure 9**. These two pathways are the most significant for the series currently studied based on the rates predicted by the ABF model. The phenyl radical pathway is slightly slower than the A2 radical pathway but this channel is a culmination of multiple pathways to form the A2 radical. The selected reaction rate profiles for benzene and naphthalene show a modest sensitivity to flame temperature and equivalence ratio.

A common soot inception model is to consider pyrene dimerization as the effective onset of soot particles (Frenklach, 2002; Wang, 2011; Totton et al., 2012; Zhang et al., 2014). The ABF model considers four major pathways, summarized in **Figure 10**, to form pyrene all stemming from phenanthrene species.

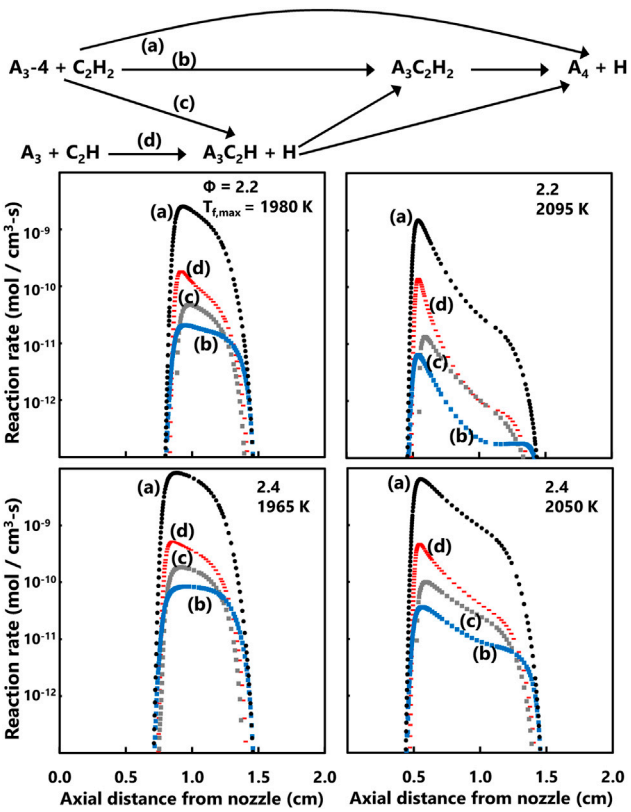

FIGURE 10 | Reaction pathways for production of pyrene (A4) considered by the ABF model **(top)** and axial profiles of computed reaction rates for four main pyrene production pathways **(bottom)**.

Phenanthrene radical (A_3-4) is postulated to combine with acetylene to either form pyrene directly or to form radicals with

unclosed rings. Phenanthrene can also react with C_2H radical to form an unclosed ring. For the current series of flames, the ABF model predicts that the direct formation of pyrene from the phenanthrene radical is an order of magnitude faster than the other pathways. Increasing flame temperature also results in somewhat lower rates of pyrene production. The species and reaction rate profiles provide insight into the underlying soot precursor flame chemistry. The experimental PSDF provide a guide for future soot formation modeling in these premixed, enriched air methane flames.

CONCLUSION

Measured PSDF of ultrafine particulate matter formed in premixed methane – air flames are examined with complementary flame structure computations. Relatively high flame temperatures are investigated by using oxygen enrichment and premixed stretch-stabilized flames. For a given equivalence ratio, the measured distribution decreases in median mobility particle size as the maximum flame temperature increases from approximately 1,950–2,050 K. The lowest equivalence ratio, highest temperature flame condition corresponds to a PSDF having a median mobility diameter of 3 nm while the highest equivalence ratio, lowest flame temperature condition corresponds to 20 nm. The soot number density shows a broad peak on the order of 10^{10} cm^{-3} for the higher equivalence ratio conditions and decreases to 10^8 for the lowest equivalence ratio. The measured soot volume fraction shows a monotonic decrease with increasing flame temperature from 10^{-7}.

Flame structure computations are carried out using detailed gas-phase combustion chemistry of the Appel, Bockhorn, Frenklach (ABF) model to examine the connection of the observed PSDF to soot precursor chemistry. Agreement between measured and computed flame standoff distances indicates that the ABF model could provide a reasonable prediction of the flame temperature and soot precursor formation for the flames currently studied. To the first order, the trends observed in the measured PSDF could be understood in terms of the computed trends for the formation of benzene, naphthalene and other soot precursors. Propargyl recombination is the dominant pathway to benzene formation for the current methane flames. According to the ABF model, naphthalene formation occurs by combination of phenyl radical + C_4H_4 and other pathways leading to naphthalene radical formation. Pyrene formation is predicted to be fastest through direct formation after combination of phenanthrene radical and acetylene. Results of the current study inform particulate matter behavior for methane and natural gas combustion applications at elevated temperature and oxygen enriched conditions.

DATA AVAILABILITY STATEMENT

The raw data supporting the conclusions of this article will be made available by the authors, without undue reservation.

AUTHOR CONTRIBUTIONS

SD: Conceptualization, methodology, software, investigation, writing—original draft, writing—review and editing, visualization, funding acquisition. JC: Conceptualization, methodology, investigation, writing—original draft, writing—review and editing, visualization, funding acquisition.

FUNDING

The work was supported by NSF Combustion and Fire Systems program under Award 1841357.

ACKNOWLEDGMENTS

Kaylin Dones Sabado aided in the flame collection of the flame images.

REFERENCES

Abid, A. D., Camacho, J., Sheen, D. a., and Wang, H. (2009). Evolution of Soot Particle Size Distribution Function in Burner-Stabilized Stagnation n-Dodecane–Oxygen–Argon Flames. *Energy Fuels* 23, 4286–4294. doi:10.1021/ef900324e

Abid, A. D., Camacho, J., Sheen, D. A., and Wang, H. (2009). Quantitative measurement of soot particle size distribution in premixed flames - The burner-stabilized stagnation flame approach. *Combustion and Flame* 156, 1862–1870. doi:10.1016/j.combustflame.2009.05.010

Abid, A. D., Heinz, N., Tolmachoff, E. D., Phares, D. J., Campbell, C. S., and Wang, H. (2008). On evolution of particle size distribution functions of incipient soot in premixed ethylene-oxygen-argon flames. *Combustion and Flame* 154, 775–788. doi:10.1016/j.combustflame.2008.06.009

Alfè, M., Apicella, B., Rouzaud, J.-N., Tregrossi, A., and Ciajolo, A. (2010). The effect of temperature on soot properties in premixed methane flames. *Combustion and Flame* 157, 1959–1965. doi:10.1016/j.combustflame.2010.02.007

Appel, J., Bockhorn, H., and Frenklach, M. (2000). Kinetic modeling of soot formation with detailed chemistry and physics: laminar premixed flames of C2 hydrocarbons. *Combustion and Flame* 121, 122–136. doi:10.1016/S0010-2180(99)00135-2

Bartos, D., Sirignano, M., Dunn, M. J., D'Anna, A., and Masri, A. R. (2019). Soot inception in laminar coflow diffusion flames. *Combustion and Flame* 205, 180–192. doi:10.1016/j.combustflame.2019.03.026

Bergthorson, J. M. (2005). *Experiments and Modeling of Impinging Jets and Premixed Hydrocarbon Stagnation Flames*. California: California Institute of Technology.

Böhm, H., Hesse, D., Jander, H., Lüers, B., Pietscher, J., Wagner, H. G. G., et al. (1989). The influence of pressure and temperature on soot formation in premixed flames. *Symp. (International) Combustion* 22, 403–411. doi:10.1016/S0082-0784(89)80047-5

Bonpua, J., Yagües, Y., Aleshin, A., Dasappa, S., and Camacho, J. (2019). Flame temperature effect on sp2 bonds on nascent carbon nanoparticles formed in premixed flames (T>2100 K): A Raman spectroscopy and particle mobility sizing study, Proc. *Combust. Inst.* 37, 943–951. doi:10.1016/j.proci.2018.06.124

Bowal, K., Martin, J. W., Misquitta, A. J., and Kraft, M. (2019). Ion-Induced Soot Nucleation Using a New Potential for Curved Aromatics. *Combustion Sci. Tech.* 191, 747–765. doi:10.1080/00102202.2019.1565496

Cain, J. P., Camacho, J., Phares, D. J., Wang, H., and Laskin, A. (2011). Evidence of aliphatics in nascent soot particles in premixed ethylene flames. *Proc. Combustion Inst.* 33, 533–540. doi:10.1016/j.proci.2010.06.164

Camacho, J., Lieb, S., and Wang, H. (2013). Evolution of size distribution of nascent soot in n- and i-butanol flames. *Proc. Combustion Inst.* 34, 1853–1860. doi:10.1016/j.proci.2012.05.100

Camacho, J., Liu, C., Gu, C., Lin, H., Huang, Z., Tang, Q., et al. (2015). Mobility size and mass of nascent soot particles in a benchmark premixed ethylene flame. *Combustion and Flame* 162, 3810–3822. doi:10.1016/j.combustflame.2015.07.018

Camacho, J., Singh, A. V., Wang, W., Shan, R., Yapp, E. K. Y., Chen, D., et al. (2017). Soot particle size distributions in premixed stretch-stabilized flat ethylene-oxygen-argon flames. *Proc. Combustion Inst.* 36, 1001–1009. doi:10.1016/j.proci.2016.06.170

Camacho, J., Tao, Y., and Wang, H. (2015). Kinetics of nascent soot oxidation by molecular oxygen in a flow reactor. *Proc. Combustion Inst.* 35, 1887–1894. doi:10.1016/j.proci.2014.05.095

Carbone, F., Attoui, M., and Gomez, A. (2016). Challenges of measuring nascent soot in flames as evidenced by high-resolution differential mobility analysis. *Aerosol Sci. Tech.* 50, 740–757. doi:10.1080/02786826.2016.1179715

Carbone, F., Gleason, K., and Gomez, A. (2017). Probing gas-to-particle transition in a moderately sooting atmospheric pressure ethylene/air laminar premixed flame. Part I: gas phase and soot ensemble characterization. *Combustion and Flame* 181, 315–328. doi:10.1016/j.combustflame.2017.01.029

Carbone, F., Moslih, S., and Gomez, A. (2017). Probing gas-to-particle transition in a moderately sooting atmospheric pressure ethylene/air laminar premixed flame. Part II: Molecular clusters and nascent soot particle size distributions. *Combustion and Flame* 181, 329–341. doi:10.1016/j.combustflame.2017.02.021

Commodo, M., Tessitore, G., De Falco, G., Bruno, A., Minutolo, P., and D'Anna, A. (2015). Further details on particle inception and growth in premixed flames. *Proc. Combustion Inst.* 35, 1795–1802. doi:10.1016/j.proci.2014.06.004

D'Alessio, A., Barone, A. C., Cau, R., D'Anna, A., and Minutolo, P. (2005). Surface deposition and coagulation efficiency of combustion generated nanoparticles in the size range from 1 to 10nm. *Proc. Combust. Inst.* 30, 2595–2603. doi:10.1016/j.proci.2004.08.267

D'Anna, A., Sirignano, M., Commodo, M., Pagliara, R., and Minutolo, P. (2008). An Experimental and Modelling Study of Particulate Formation in Premixed Flames Burning Methane. *Combust. Sci. Technol.* 180, 950–958. doi:10.1080/00102200801894448

Dasappa, S., and Camacho, J. (2021). Evolution in size and structural order for incipient soot formed at flame temperatures greater than 2100 Kelvin. *Fuel* 291, 120196. doi:10.1016/j.fuel.2021.120196

Dasappa, S., and Camacho, J. (2020). Formation of nanocrystalline manganese oxide in flames: oxide phase governed by classical nucleation and size-dependent equilibria. *CrystEngComm* 22, 5509–5521. doi:10.1039/D0CE00734J

Dasappa, S., and Camacho, J. (2021). Fuel molecular structure effect on soot mobility size in premixed C6 hydrocarbon flames. *Fuel* 300, 120973. doi:10.1016/j.fuel.2021.120973

Dasappa, S., and Camacho, J. (2021). Raman spectroscopy, mobility size and radiative emissions data for soot formed at increasing temperature and equivalence ratio in flames hotter than conventional combustion applications. *Data in Brief* 36, 107064. doi:10.1016/j.dib.2021.107064

Dasappa, S., and Camacho, J. (2021). Thermodynamic Barrier to Nucleation for Manganese Oxide Nanoparticles Synthesized by High-Temperature Gas-to-Particle Conversion. *Energy Fuels* 35, 1874–1884. doi:10.1021/acs.energyfuels.0c03662

Desgroux, P., Faccinetto, A., Mercier, X., Mouton, T., Aubagnac Karkar, D., and El Bakali, A. (2017). Comparative study of the soot formation process in a "nucleation" and a "sooting" low pressure premixed methane flame. *Combustion and Flame* 184, 153–166. doi:10.1016/j.combustflame.2017.05.034

Frenklach, M., Clary, D. W., Gardiner, W. C., and Stein, S. E. (1985). Detailed kinetic modeling of soot formation in shock-tube pyrolysis of acetylene. *Symp. (International) Combustion* 20, 887–901. doi:10.1016/S0082-0784(85)80578-6

Frenklach, M. (2002). Reaction mechanism of soot formation in flames. *Phys. Chem. Chem. Phys.* 4, 2028–2037. doi:10.1039/B110045A

Gleason, K., Carbone, F., Sumner, A. J., Drollette, B. D., Plata, D. L., and Gomez, A. (2021). Small aromatic hydrocarbons control the onset of soot nucleation. *Combustion and Flame* 223, 398–406. doi:10.1016/j.combustflame.2020.08.029

Gu, C., Lin, H., Camacho, J., Lin, B., Shao, C., Li, R., et al. (2016). Particle size distribution of nascent soot in lightly and heavily sooting premixed ethylene flames. *Combustion and Flame* 165, 177–187. doi:10.1016/j.combustflame.2015.12.002

Haynes, B. S., and Wagner, H. G. (1981). Soot formation. *Prog. Energ. Combustion Sci.* 7, 229–273. doi:10.1016/0360-1285(81)90001-0

Heywood, J. B. (2018). *Internal Combustion Engine Fundamentals*. New York: McGraw-Hill.

Jacobson, M. C., Hansson, H.-C., Noone, K. J., and Charlson, R. J. (2000). Organic atmospheric aerosols: Review and state of the science. *Rev. Geophys.* 38, 267–294. doi:10.1029/1998RG000045

Jacobson, M. Z. (2001). Strong radiative heating due to the mixing state of black carbon in atmospheric aerosols. *Nature* 409, 695–697. doi:10.1038/35055518

Brunnenmeyer, J., and Camacho, J., Calculation of 2D Flame Structure for Premixed Axisymmetric Stagnation Flames with Elevated Flame Temperature and Equivalence Ratio, in: *AIAA Scitech 2019 Forum*, American Institute of Aeronautics and Astronautics, USA, (2019). doi:10.2514/6.2019-0781

Johansson, K. O., Head-Gordon, M. P., Schrader, P. E., Wilson, K. R., and Michelsen, H. A. (2018). Resonance-stabilized hydrocarbon-radical chain reactions may explain soot inception and growth. *Science* 361, 997–1000. doi:10.1126/science.aat3417

Kee, R. J., Miller, J. A., Evans, G. H., and Dixon-Lewis, G. (1989). A computational model of the structure and extinction of strained, opposed flow, premixed methane-air flames. *Symp. (International) Combustion* 22, 1479–1494. doi:10.1016/S0082-0784(89)80158-4

Kee, R. J., Rupley, F. M., and Miller, J. A. (1989). *Chemkin-II: A Fortran chemical kinetics package for the analysis of gas-phase chemical kinetics*. United States: OSTI. doi:10.2172/5681118

Larriba-Andaluz, C., and Carbone, F. (2021). The size-mobility relationship of ions, aerosols, and other charged particle matter. *J. Aerosol Sci.* 151, 105659. doi:10.1016/j.jaerosci.2020.105659

Law, C. K. (2006). *Combustion Physics*. Cambridge: Cambrige Press. doi:10.1017/cbo9780511754517

Li, Z., and Wang, H. (2003). Drag force, diffusion coefficient, and electric mobility of small particles. II. Application. *Phys. Rev. E.* 68, 61207. doi:10.1103/physreve.68.061207

Lin, H., Gu, C., Camacho, J., Lin, B., Shao, C., Li, R., et al. (2016). Mobility size distributions of soot in premixed propene flames. *Combustion and Flame* 172, 365–373. doi:10.1016/j.combustflame.2016.07.002

Liu, C., Camacho, J., and Wang, H. (2018). Phase Equilibrium of TiO 2 Nanocrystals in Flame-Assisted Chemical Vapor Deposition. *ChemPhysChem* 19, 180–186. doi:10.1002/cphc.201700962

Lutz, A. E., Kee, R. J., Grcar, J. F., and Rupley, F. M. (1997). *OPPDIF: A Fortan program for computing opposed-flow diffusion flames*. United States: OSTI. doi:10.2172/568983

Maricq, M. M. (2006). A comparison of soot size and charge distributions from ethane, ethylene, acetylene, and benzene/ethylene premixed flames. *Combustion and Flame* 144, 730–743. doi:10.1016/j.combustflame.2005.09.007

Maricq, M. M., Harris, S. J., and Szente, J. J. (2003). Soot size distributions in rich premixed ethylene flames. *Combustion and Flame* 132, 328–342. doi:10.1016/S0010-2180(02)00502-3

Maricq, M. M. (2004). Size and charge of soot particles in rich premixed ethylene flames. *Combustion and Flame* 137, 340–350. doi:10.1016/j.combustflame.2004.01.013

Montgomery, C. T., and Smith, M. B. (2010). Hydraulic Fracturing: History of an Enduring Technology. *J. Pet. Technol.* 62, 26–40. doi:10.2118/1210-0026-JPT

Mouton, T., Mercier, X., Wartel, M., Lamoureux, N., and Desgroux, P. (2013). Laser-induced incandescence technique to identify soot nucleation and very small particles in low-pressure methane flames. *Appl. Phys. B* 112, 369–379. doi:10.1007/s00340-013-5446-x

Pejpichestakul, W., Frassoldati, A., Parente, A., and Faravelli, T. (2018). Kinetic modeling of soot formation in premixed burner-stabilized stagnation ethylene flames at heavily sooting condition. *Fuel* 234, 199–206. doi:10.1016/j.fuel.2018.07.022

Puduppakkam, K. V., Modak, A. U., Naik, C. V., Camacho, J., Wang, H., and Meeks, E. (2014). A soot chemistry model that captures fuel effects. *Proc. ASME Turbo Expo* 4B, 11. doi:10.1115/GT2014-27123

Raj, A., Sander, M., Janardhanan, V., and Kraft, M. (2010). A study on the coagulation of polycyclic aromatic hydrocarbon clusters to determine their collision efficiency. *Combustion and Flame* 157, 523–534. doi:10.1016/j.combustflame.2009.10.003

Russo, C., Alfè, M., Rouzaud, J.-N., Stanzione, F., Tregrossi, A., and Ciajolo, A. (2013). Probing structures of soot formed in premixed flames of methane, ethylene and benzene. *Proc. Combustion Inst.* 34, 1885–1892. doi:10.1016/j.proci.2012.06.127

Saggese, C., Cuoci, A., Frassoldati, A., Ferrario, S., Camacho, J., Wang, H., et al. (2016). Probe effects in soot sampling from a burner-stabilized stagnation flame. *Combustion and Flame* 167, 184–197. doi:10.1016/j.combustflame.2016.02.013

Saggese, C., Ferrario, S., Camacho, J., Cuoci, A., Frassoldati, A., Ranzi, E., et al. (2015). Kinetic modeling of particle size distribution of soot in a premixed burner-stabilized stagnation ethylene flame. *Combustion and Flame* 162, 3356–3369. doi:10.1016/j.combustflame.2015.06.002

Saggese, C., Singh, A. V., Xue, X., Chu, C., Kholghy, M. R., Zhang, T., et al. (2019). The distillation curve and sooting propensity of a typical jet fuel. *Fuel* 235, 350–362. doi:10.1016/j.fuel.2018.07.099

Schenk, M., Lieb, S., Vieker, H., Beyer, A., Gölzhäuser, A., Wang, H., et al. (2013). Imaging Nanocarbon Materials: Soot Particles in Flames are Not Structurally Homogeneous. *ChemPhysChem* 14, 3248–3254. doi:10.1002/cphc.201300581

Seshadri, K., and Williams, F. A. (1978). Laminar flow between parallel plates with injection of a reactant at high reynolds number. *Int. J. Heat Mass Transfer* 21, 251–253. doi:10.1016/0017-9310(78)90230-2

Shaddix, C. R., and Williams, T. C. (2017). The effect of oxygen enrichment on soot formation and thermal radiation in turbulent, non-premixed methane flames. *Proc. Combustion Inst.* 36, 4051–4059. doi:10.1016/j.proci.2016.06.106

Sirignano, M., Alfè, M., Tregrossi, A., Ciajolo, A., and D'Anna, A. (2011). Experimental and modeling study on the molecular weight distribution and properties of carbon particles in premixed sooting flames. *Proc. Combustion Inst.* 33, 633–640. doi:10.1016/j.proci.2010.07.065

Sirignano, M., and D'Anna, A. (2013). Coagulation of combustion generated nanoparticles in low and intermediate temperature regimes: An experimental study. *Proc. Combustion Inst.* 34, 1877–1884. doi:10.1016/j.proci.2012.06.119

Slavinskaya, N. A., and Frank, P. (2009). A modelling study of aromatic soot precursors formation in laminar methane and ethene flames. *Combustion and Flame* 156, 1705–1722. doi:10.1016/j.combustflame.2009.04.013

Smooke, M. D., Puri, I. K., and Seshadri, K. (1988). A comparison between numerical calculations and experimental measurements of the structure of a counterflow diffusion flame burning diluted methane in diluted air. *Symp. (International) Combustion* 21, 1783–1792. doi:10.1016/S0082-0784(88)80412-0

Tang, Q., Cai, R., You, X., and Jiang, J. (2017). Nascent soot particle size distributions down to 1 nm from a laminar premixed burner-stabilized stagnation ethylene flame. *Proc. Combustion Inst.* 36, 993–1000. doi:10.1016/j.proci.2016.08.085

Totton, T. S., Misquitta, A. J., and Kraft, M. (2012). A quantitative study of the clustering of polycyclic aromatic hydrocarbons at high temperatures. *Phys. Chem. Chem. Phys.* 14, 4081–4094. doi:10.1039/C2CP23008A

TSI (2019). *Diffusion correction using TSI's 1 nm SMPS SYSTEM Model 3938, Application note SMPS-010.* US: TSI.

Von Karman, T. (1921). On laminar and turbulent friction. *NACA Tech. Memo.*, 1092.

Wang, H. (2011). Formation of nascent soot and other condensed-phase materials in flames. *Proc. Combustion Inst.* 33, 41–67. doi:10.1016/j.proci.2010.09.009

Wang, Y., Fang, J., Attoui, M., Chadha, T. S., Wang, W.-N., and Biswas, P. (2014). Application of Half Mini DMA for sub 2nm particle size distribution measurement in an electrospray and a flame aerosol reactor. *J. Aerosol Sci.* 71, 52–64. doi:10.1016/j.jaerosci.2014.01.007

Xu, F., Sunderland, P. B., and Faeth, G. M. (1997). Soot formation in laminar premixed ethylene/air flames at atmospheric pressure. *Combustion and Flame* 108, 471–493. doi:10.1016/S0010-2180(96)00200-3

Yapp, E. K. Y., Chen, D., Akroyd, J., Mosbach, S., Kraft, M., Camacho, J., et al. (2015). Numerical simulation and parametric sensitivity study of particle size distributions in a burner-stabilised stagnation flame. *Combustion and Flame* 162, 2569–2581. doi:10.1016/j.combustflame.2015.03.006

Zhang, H.-B., You, X., Wang, H., and Law, C. K. (2014). Dimerization of Polycyclic Aromatic Hydrocarbons in Soot Nucleation. *J. Phys. Chem. A.* 118, 1287–1292. doi:10.1021/jp411806q

Zhao, B., Yang, Z., Wang, J., Johnston, M. V., and Wang, H. (2003). Analysis of Soot Nanoparticles in a Laminar Premixed Ethylene Flame by Scanning Mobility Particle Sizer. *Aerosol Sci. Tech.* 37, 611–620. doi:10.1080/02786820300908

Conflict of Interest: The authors declare that the research was conducted in the absence of any commercial or financial relationships that could be construed as a potential conflict of interest.

Publisher's Note: All claims expressed in this article are solely those of the authors and do not necessarily represent those of their affiliated organizations, or those of the publisher, the editors and the reviewers. Any product that may be evaluated in this article, or claim that may be made by its manufacturer, is not guaranteed or endorsed by the publisher.

Copyright © 2021 Dasappa and Camacho. This is an open-access article distributed under the terms of the Creative Commons Attribution License (CC BY). The use, distribution or reproduction in other forums is permitted, provided the original author(s) and the copyright owner(s) are credited and that the original publication in this journal is cited, in accordance with accepted academic practice. No use, distribution or reproduction is permitted which does not comply with these terms.